TRF2 rescues pathogenic phenotypes in Duchenne muscular dystrophy cardiomyocytes derived from human iPSCs

Asuka Eguchi[1,2,3], Sofía I. Torres-Bigio[1,3], Kassie Koleckar[1], Foster Birnbaum[1], and Helen M. Blau[1,2,3]

1. Baxter Laboratory for Stem Cell Biology, Department of Microbiology and Immunology, Stanford School of Medicine, Stanford, CA 94305
2. Institute for Stem Cell Biology and Regenerative Medicine, Stanford University School of Medicine, Stanford CA 94305
3. Stanford Cardiovascular Institute, Stanford University School of Medicine, Stanford, CA 94305

Abstract

Duchenne muscular dystrophy (DMD) is a severe muscle wasting disease caused by the lack of dystrophin. Heart failure, driven by cardiomyocyte death, fibrosis, and the development of dilated cardiomyopathy, is the leading cause of death in DMD patients. Current treatments decrease the mechanical load on the heart; however, these treatments do not address the root cause of dilated cardiomyopathy: cardiomyocyte death. Previously, we showed that longer telomeres are protective against dilated cardiomyopathy. Here we investigated the role of telomeres as a target for therapy in DMD cardiomyocytes using human induced pluripotent stem cells (iPSCs) to model the disease. Compared to healthy controls, DMD cardiomyocytes exhibited reduced cell size, nuclear size, and sarcomere density. The telomere-binding protein, TRF2, is a core component of the shelterin complex, which protects chromosome ends. TRF2 levels are reduced relative to healthy controls in DMD cardiomyocytes. We hypothesized that decreased TRF2 drives telomere attrition and subsequent cardiomyocyte death in the progression of dilated cardiomyopathy. Our data show that TRF2 overexpression rescued deficits in cell size, nuclear size, sarcomere density, and calcium handling. These data highlight the benefits of TRF2 upregulation as a potential gene therapy to delay the onset of dilated cardiomyopathy.

Introduction

Duchenne muscular dystrophy (DMD) affects 1 out of 5,000 males and manifests as progressive muscle degeneration (1). DMD is caused by a lack of dystrophin, a large cytoskeletal protein that spans the contractile apparatus to the extracellular matrix (2). Dilated cardiomyopathy is the leading cause of death in DMD patients (3). Currently, patients are prescribed angiotensin-converting enzyme inhibitors, angiotensin II receptor blockers, and mineralocorticoid receptor antagonists that lower blood pressure as well as beta blockers that slow the heart rate (4). These strategies reduce the mechanical load on the

heart, but do not address the cardiomyocyte death and fibrosis that drive the progression of dilated cardiomyopathy.

We previously reported an intriguing link between genetic cardiomyopathies and telomere shortening. The dystrophin deficient *mdx* mouse does not manifest the characteristic symptoms of DMD. However, when crossed with an *mTR* knock-out mouse that is missing the RNA component of telomerase, mdx^{4cv}/mTR^{G2} mice exhibit hallmark DMD phenotypes, including severe muscle degeneration, kyphosis, dilated cardiomyopathy, and shortened lifespan (5–7). Mice have significantly longer telomeres than humans. This discovery suggested that long telomeres in *Mus musculus* protect them from the full-blown symptoms of human disease. Indeed, we found that telomere shortening is a common feature in cardiomyocytes from tissues of patients with cardiomyopathies caused by mutations in genes that encode sarcomeric or cytoskeletal proteins, including dystrophin (8). Furthermore, crossing mice heterozygous for *Notch1* with *mTR* knock-out mice revealed cardiovascular disease phenotypes, including premature calcification of the aortic valve, that would not have otherwise manifested in *Notch1* haplosufficient mice, underscoring the role of long telomeres as being cardioprotective (9).

We and others have capitalized on human induced pluripotent stem cells (iPSCs) to model disease phenotypes in a dish in order to circumvent differences between human and mouse cells (8, 10–12). In this study, we use three DMD iPSC lines with matching isogenic healthy controls and draw conclusions based on consistent differences we observe in multiple lines. By using isogenic controls, we ensure that we control for genetic background and that the differences we observe between healthy and diseased states can be attributed to the dystrophin deficiency. We recently reported that DMD cardiomyocytes differentiated from iPSCs (iPSC-CMs) exhibit aberrant calcium handling, impaired contractile function, and shortened telomeres, leading to a DNA damage response (10). Here we extend these studies on DMD iPSC-CMs as a disease model by further characterizing morphological deficiencies of DMD iPSC-CMs. We then validate a lentiviral reporter system to enrich for a pure population of cardiomyocytes and test whether a telomere-binding protein can protect the telomeres and rescue the pathogenic characteristics we observe in DMD iPSC-CMs. Our results highlight a therapeutic strategy, increased expression of the telomere-binding protein, TRF2, to ameliorate pathogenic characteristics of DMD cardiomyocytes. This therapeutic strategy has the potential to universally address all DMD mutations.

Results

DMD iPSC as a Disease Model. We differentiated human induced pluripotent stem cells (iPSCs) to cardiomyocytes to model Duchenne muscular dystrophy phenotypes (Table 1 and Fig. 1*A*). DMD can be caused by a wide variety of mutations that impact the function of the dystrophin protein (13). Two lines, DMD19 and DMD16, were derived from patients with nonsense mutations in the dystrophin gene (14, 15). Both lines have been CRISPR-corrected to generate corresponding isogenic controls, DMD19 iso and DMD16 iso, in which the dystrophin mutations are corrected (14, 15). One line, UC3.4, was derived from

a healthy patient, and the isogenic DMD line, UC1015.6, was CRISPR-induced to yield the mutation, c.263delG (16, 17). This mutation results in deletion of the N-terminus of dystrophin that renders the truncated protein dysfunctional (16, 17). Importantly, the lack of the N-terminal actin-binding domain of dystrophin is associated with early onset dilated cardiomyopathy (18). The use of three DMD iPSC lines with matching isogenic healthy controls ensure that we control for genetic background, and any consistent differences we observe between healthy and diseased states can be attributed to the dystrophin deficiency. All three lines expressed pluripotency markers, OCT4, SOX2, and TRA-1-60, in the iPSC state (*SI Appendix*, Fig. S1*A*-*C*). We differentiated the iPSCs to cardiomyocytes using established protocols (19), then purified the iPSC-CMs by culturing in media lacking glucose and supplemented with lactate, a method that starves contaminating fibroblasts (20). On Day 30, we observed cardiac troponin T (cTnT) staining in the iPSC-CMs (Fig. 1*B*). We also immunostained for dystrophin and observed expression along the sarcomeres in the healthy control lines, UC3.4, DMD19 iso, and DMD16 iso (Fig. 1*B*). The DMD lines, DMD19 and DMD16, did not show dystrophin expression along the sarcomeres as they harbor nonsense mutations (Fig. 1*B*) (15). The UC1015.6 line has a mutation that induces the expression of a truncated dystrophin lacking a large portion of the N-terminal domain that binds actin filaments (17). Immunostaining with the ab15277 antibody that recognizes the C-terminus of dystrophin detected the truncated dystrophin in the DMD line, UC1015.6 (Fig. 1*B*), and use of the MANEX1A antibody that recognizes the N-terminus showed a lack of expression (*SI Appendix*, Fig. S2), consistent with the report that this line expresses a dystrophin variant missing the N-terminal actin-binding domain (17). All lines, healthy and DMD alike, showed nuclear staining with the C-terminal antibody. The ubiquitously expressed Dp71 isoform, expressed in human heart tissue and in iPSC-CMs (15, 21, 22), is the protein form likely recognized as none of the mutations we use here preclude expression of this isoform. Our characterization of the iPSC-CMs demonstrating expression of cardiac-specific markers and muscle-specific dystrophin deficiency in the diseased cells validated use of these lines as robust disease models to study the role of telomeres in the progression of DMD.

Table 1. iPSC lines and mutational status

Category	Name	Mutation Type	Description	Reference
Control	DMD19 iso	None	Isogenic control of DMD19	(14, 15)
DMD	DMD19	Patient-derived	DMD (c.4918_4919delACinsTG)	(14, 15)
Control	DMD16 iso	None	Isogenic control of DMD16	(14, 15)
DMD	DMD16	Patient-derived	DMD (c.10171C>T)	(14, 15)
Control	UC3.4	None	Isogenic control of UC1015.6	(16, 17)
DMD	UC1015.6	CRISPR-induced	DMD (c.263delG)	(16, 17)

DMD iPSC-CMs Exhibit Morphological Deficits. Previously, we reported that DMD iPSC-CMs exhibit impaired contractile function on stiff substrates mimicking a fibrotic myocardium as well as poor calcium handling (10). We investigated the morphological deficits that could potentially account for these functional shortcomings. On Day 30 of differentiation, we observed that DMD iPSC-CMs were smaller in cell size and were comprised of smaller nuclei (Fig. 2*A*-*I*). The reduced cell size is consistent with our

previous report where we seeded iPSC-CMs on 2,000 μm^2 micropatterns of extracellular matrix with a length:width aspect ratio of 7:1 (10), a regime that has been shown to promote iPSC-CM maturation (23, 24). When cultured in monolayers without any physical constraints, the difference in cell sizes were more pronounced. DMD iPSC-CMs were 43-80% the size of the healthy iPSC-CMs (Fig. 2*D-F*). Strikingly, in *mdx^{4cv}/mTR^{G2}* mice, we also observed reduced cardiomyocyte diameter and smaller nuclei in the hearts of the mouse model that phenocopies severe symptoms observed in Duchenne patients (6). The sarcomere density as measured by cTnT signal over cell area was also reduced in DMD iPSC-CMs compared to isogenic controls (Fig. 2*J-L*). This decrease in cTnT levels was independent of cell size, indicating that DMD iPSC-CMs are both smaller and have fewer myofibrils. The reduced myofibril content likely accounts for the reduced force of contraction, contraction velocity, and relaxation velocity previously

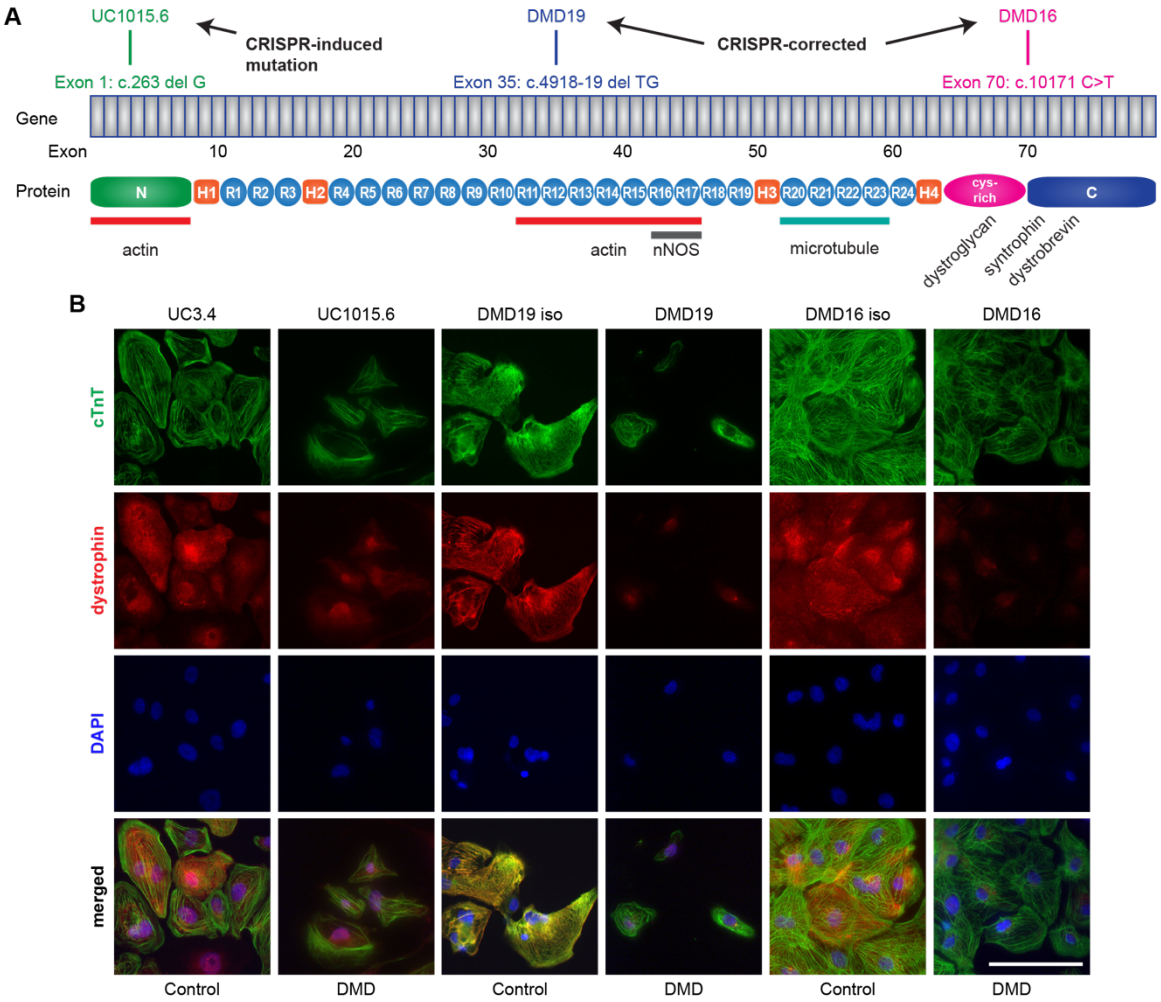

Figure 1. Cardiomyocytes differentiated from dystrophin-deficient induced pluripotent stem cells. (*A*) Schematic of dystrophin gene and the mutations corresponding to the cell lines. The UC1015.6 line harbors a CRISPR-induced mutation that results in expression of a truncated dystrophin missing the N-terminus. DMD19 and DMD16 are patient-derived iPSCs that have nonsense mutations. (*B*) Cardiac troponin T (cTnT) and dystrophin immunostaining in Day 30 iPSC-CMs. The antibody for dystrophin (ab15277) recognizes the C-terminus of dystrophin. DAPI in blue marks nuclei. Scale bar = 100 μm.

measured in these DMD iPSC-CMs (10). Importantly, our findings are consistent with electron micrographs that showed sparse myofibril content in the hearts of DMD patients (25). The reduced cell size, nuclear size, and sarcomere density was statistically significant in all three lines of DMD iPSC-CMs when compared with the healthy isogenic controls, underscoring the consistency of these results. Collectively, the morphological deficits of DMD iPSC-CMs suggest that their smaller cell size as well as reduced myofibril content impairs their ability to contract like healthy cells.

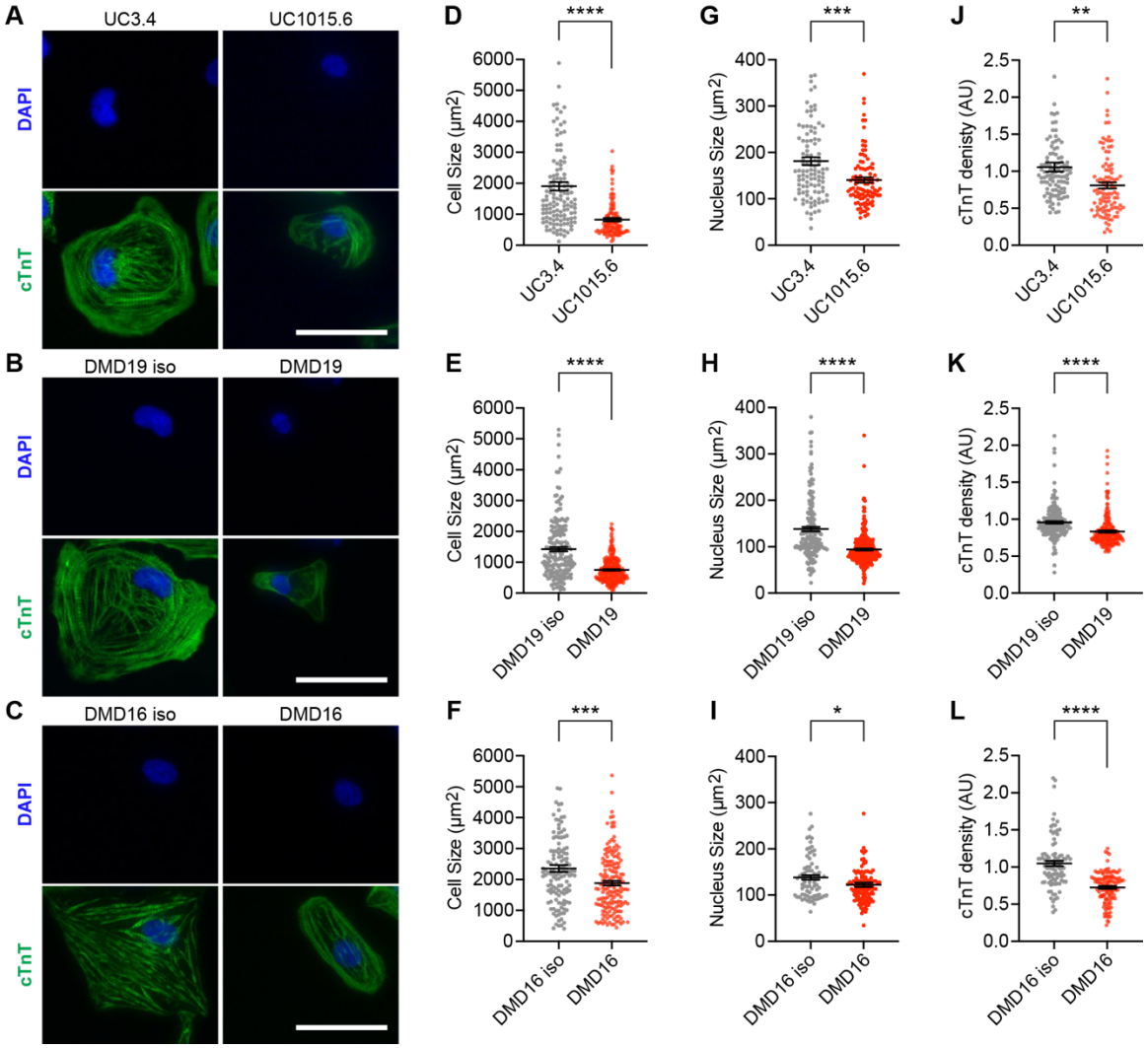

Figure 2. DMD iPSC-CMs exhibit deficits in cell size, nuclear size, and sarcomere density on Day 30 of differentiation. Cardiac troponin T (cTnT) immunostaining and DAPI staining for nuclei in (*A*) UC3.4 and UC1015.6 iPSC-CMs, (*B*) DMD19 iso and DMD19 iPSC-CMs, and (*C*) DMD16 iso and DMD16 iPSC-CMs. Scale bar = 50 µm. Area of cells for (*D*) UC3.4 and UC1015.6 iPSC-CMs, (*E*) DMD19 iso and DMD19 iPSC-CMs, and (*F*) DMD16 iso and DMD16 iPSC-CMs. Nuclear size for (*G*) UC3.4 and UC1015.6 iPSC-CMs, (*H*) DMD19 iso and DMD19 iPSC-CMs, and (*I*) DMD16 iso and DMD16 iPSC-CMs. Sarcomere density as measured by cTnT signal over cell area for (*J*) UC3.4 and UC1015.6 iPSC-CMs, (*K*) DMD19 iso and DMD19 iPSC-CMs, and (*L*) DMD16 iso and DMD16 iPSC-CMs. Cells were scored from 3 differentiation experiments. N = 97-205 cells. Data shown are mean ± SEM. One-way ANOVA and Tukey test for post-hoc comparison was used to determine significance. * $p < 0.05$, ** $p < 0.01$, *** $p < 0.001$, and **** $p < 0.0001$.

TRF2 Overexpression in DMD iPSC-CMs. Previously, we reported that DMD iPSC-CMs have shortened telomeres compared to healthy controls and activation of the DNA damage response occurs concomitantly (8, 10). When we measured telomeric repeat-binding factor 2 (TRF2) levels by western blot, we found that DMD iPSC-CMs express lower levels of TRF2 compared to isogenic controls (*SI Appendix*, Fig. S3*A*). We tested whether overexpression of TRF2, which inhibits the ataxia-telangiectasia-mutated (ATM)-mediated DNA damage response (26, 27), could rescue telomere attrition in DMD iPSC-CMs. To further enrich for a pure population of cardiomyocytes beyond glucose starvation, we developed a lentiviral reporter system that expresses the zeocin resistance gene (Zeo^R) under the control of the human cTnT promoter (28, 29). As a proof-of-concept, we first tested the reporter system that encodes enhanced green fluorescent protein (EGFP) and Zeo^R separated by a T2A self-cleaving peptide (*SI Appendix*, Fig. S2*B*). Colocalization of EGFP with cTnT immunostaining demonstrated that the reporter system provides a reliable method to obtain a pure population of cardiomyocytes (*SI Appendix*, Fig. S2*C*). For subsequent purifications, we used a cTnT reporter that expresses Zeo^R alone that enables purification by zeocin selection (*SI Appendix*, Fig. S2*D*). By combining glucose starvation with zeocin selection, we capitalized on two orthogonal purification methods to ensure measurement of telomeres in the cardiomyocyte population. On day 10 of differentiation, we transduced DMD iPSC-CMs with TRF2. As a negative control for retroviral transduction, we used an Empty retroviral control, comprised of no open reading frame. While TRF2 protein levels were quite low in the differentiated healthy and DMD iPSC-CMs, when overexpressed, TRF2 levels were elevated significantly in DMD iPSC-CMs (*SI Appendix*, Fig. S3*B-C*). Following TRF2 overexpression, we observed attenuated levels of phospho-CHK2, the checkpoint effector kinase that is activated in response to double-stranded breaks, in DMD iPSC-CMs (*SI Appendix*, Fig. S3*D-E*). In comparison to hydrogen peroxide-treated iPSCs, which induces strong activation of CHK2 kinase (*SI Appendix*, Fig. S3*D*), levels of phospho-CHK2 were lower in DMD iPSC-CMs, but consistently attenuated by TRF2 overexpression (*SI Appendix*, Fig. S3*D-E*). In comparison to highly proliferative iPSCs, only 0.4-2.5% of iPSC-CMs incorporate EdU and thus, undergo DNA replication checkpoint surveillance by CHK2 (*SI Appendix*, Fig. S4*A-G*). Therefore, the 1.5 to 2-fold difference in levels of phospho-CHK2 observed in DMD iPSC-CMs with and without TRF2 overexpression suggests protection of telomeres by TRF2 and inhibition of the DNA damage response. Intriguingly, the role of telomeres in the demise of cardiomyocytes may extend beyond DMD as reduced TRF2 levels and telomere shortening have been observed in the hearts of patients with idiopathic and ischemic dilated cardiomyopathy (30). Complementary to our findings, overexpression of a dominant negative mutant of TRF2 or knocking down TRF2 with an antisense oligonucleotide resulted in CHK2 activation and telomere shortening in cardiomyocytes isolated from rats (30). Thus, protection of telomeres with TRF2 may be relevant to other cardiomyopathies beyond those caused by dystrophin deficiency where telomere attrition is a hallmark of disease progression.

TRF2 Rescues Deficits in Cell Morphology and Calcium Handling. DMD iPSC-CMs exhibit decreased cell size, nuclear size, and sarcomere density compared to their healthy counterparts (Fig. 2*A-L*). When

we assayed for morphological phenotypes associated with DMD iPSC-CMs, unexpectedly, we discovered that TRF2 improved cell size and nuclear size in all three DMD lines (Fig. 3*A-I*). TRF2 overexpression also significantly increased the density of cTnT in UC1015.6 and DMD19 iPSC-CMs to levels that were statistically significant (Fig. 3*J-L*). The increase in cTnT protein levels were validated by western blot in the DMD19 line (*SI Appendix*, Fig. S3*F*).

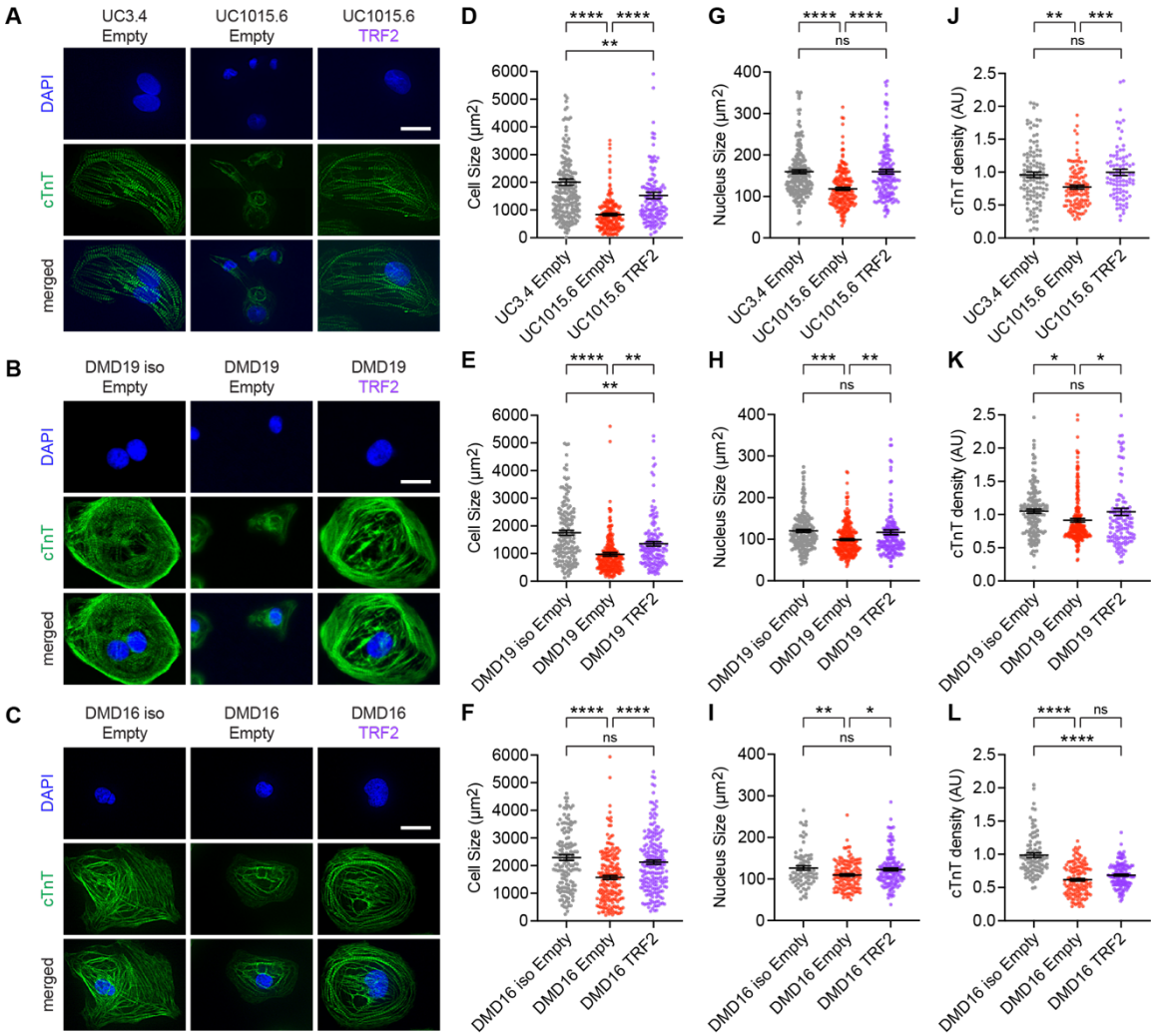

Figure 3. TRF2 rescues deficits in cell size, nuclear size, and sarcomere density. Cells were transduced with TRF2 or an empty lentiviral control on Day 10 and assayed on Day 30. Cardiac troponin T (cTnT) immunostaining and DAPI staining for nuclei in (*A*) UC iPSC-CMs, (*B*) DMD19 iPSC-CMs, and (*C*) DMD16 iPSC-CMs. Scale bar = 20 µm. Area of cells for (*D*) UC iPSC-CMs, (*E*) DMD19 iPSC-CMs, and (*F*) DMD16 iPSC-CMs. Nuclear size for (*G*) UC iPSC-CMs, (*H*) DMD19 iPSC-CMs, and (*I*) DMD16 iPSC-CMs. Sarcomere density as measured by cTnT signal over cell area for (*J*) UC iPSC-CMs, (*K*) DMD19 iPSC-CMs, and (*L*) DMD16 iPSC-CMs. Cells were scored from 3 differentiation experiments. N = 90-230 cells. Data shown are mean ± SEM. One-way ANOVA and Tukey test for post-hoc comparison was used to determine significance. * $p < 0.05$, ** $p < 0.01$, *** $p < 0.001$, and **** $p < 0.0001$.

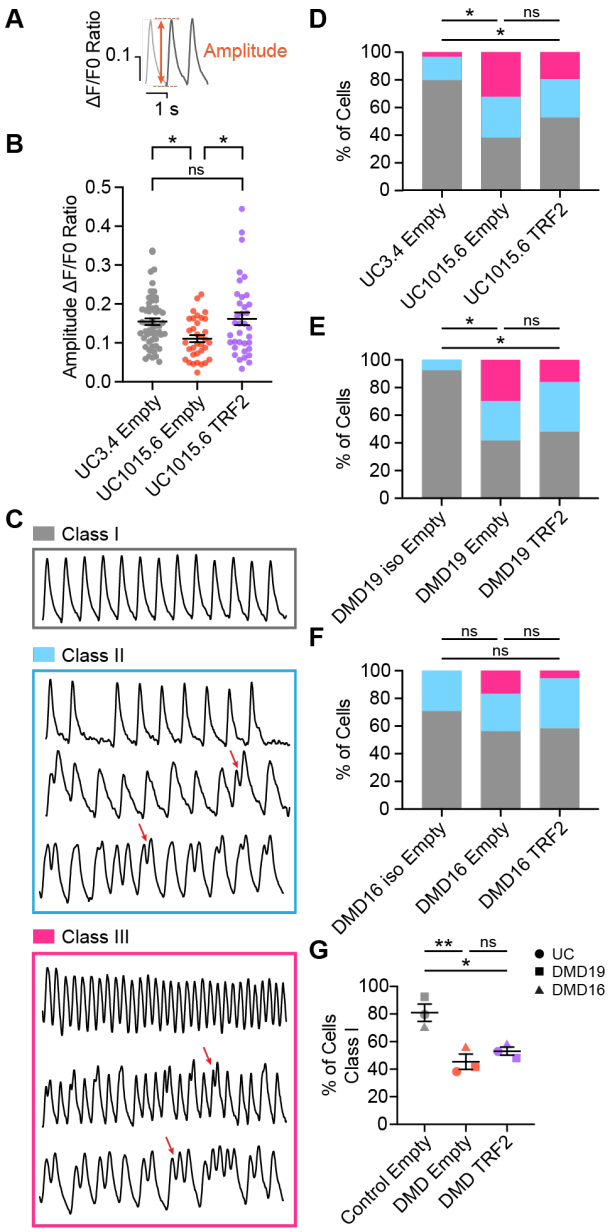

Figure 4. TRF2 partially rescues aberrant calcium handling in DMD iPSC-CMs. Cells were transduced with TRF2 or an empty retroviral control on Day 10 and assayed on Day 30. (*A*) Amplitude is the difference between the maximum and minimum calcium ratio. (*B*) Amplitude for UC iPSC-CMs. (*C*) Class I – traces with regular peaks at 1-second intervals, Class II – traces that deviate slightly from the 1-second intervals and show signs of early afterdepolarization, and Class III – traces that deviate significantly from the 1-second intervals. Examples of early afterdepolarization events are indicated by the red arrows. Calcium traces categorized into these classes for (*D*) UC iPSC-CMs, (*E*) DMD19 iPSC-CMs, and (*F*) DMD16 iPSC-CMs. Pearson's chi-square test followed by z-test with Bonferroni correction was used for pairwise comparisons. *$p < 0.05$. See *SI Appendix*, Table S1 for z-scores. (*G*) Percentage of cells with Class I calcium transients from each iPSC line. Percentages of cells in each class were scored from 3-6 differentiation experiments. Calcium imaging was performed on 24-77 cells per condition. Cells were paced at 1 Hz. Data shown are mean ± SEM. One-way ANOVA and Tukey test for post-hoc comparison was used to determine significance. * $p < 0.05$ and ** $p < 0.01$.

In DMD cardiomyocytes, dystrophin deficiency leads to a leaky plasma membrane that causes elevated calcium levels and poor calcium handling. To evaluate the effect of TRF2 on cardiomyocyte function, we performed calcium imaging using the ratiometric calcium dye, Fura Red AM. We micropatterned iPSC-CMs at a 7:1 length:width aspect ratio on glass-bottomed wells (*SI Appendix*, Fig. S4*A*), a bioengineering method that promotes parallel alignment of the myofibrils and improves the maturity of iPSC-CMs (10, 23, 24). TRF2 transduction restored the transient amplitude for UC1015.6 iPSC-CMs to levels comparable to the healthy isogenic control, UC3.4 iPSC-CMs, under conditions of pacing at 1 Hz (Fig. 4*A*-*B*). While other parameters of calcium handling, including time to peak, peak duration, and peak frequency, showed a partial rescue, none improved to statistically significant levels (*SI Appendix*, Fig. S4*B*-*M*). There were significant differences between healthy controls and DMD iPSC-CMs for the UC and DMD19 lines, consistent with our previous study characterizing calcium handling in these cells (10). Next, we characterized the types of traces for each cell as Class I (traces with regular peaks at 1-second intervals), Class II (traces that deviate slightly from the 1-second intervals and show signs of early afterdepolarization), and Class III (traces that deviate significantly from the 1-second intervals) (Fig. 4*C*). Early afterdepolarization events show calcium spikes within the decay phase of the calcium transients and can cause lethal arrhythmias (31), and correction of such events would have a meaningful impact on preventing heart failure. As the iPSC-CMs are paced at 1 Hz, calcium transients should oscillate at regular 1-second intervals. Indeed, for the healthy control iPSC-CMs, the majority of cells exhibited Class I traces (Fig. 4*D*-*F*). For the UC and DMD19 lines, DMD iPSC-CMs showed significantly higher frequencies of aberrant calcium handling of Class II and III trace types (Fig. 4*D*-*F* and *SI Appendix*, Table S1). Transduction with TRF2 in DMD iPSC-CMs increased the percentage of cells exhibiting healthy Class I traces from 45.4 ± 5.6% to 53.0 ± 3.0%; however, this increase was not statistically significant (Fig 4*G*). Taken together, TRF2 overexpression led to consistent and robust rescue of cell size, nuclear size, and sarcomere density in all three DMD lines. Calcium imaging demonstrated partial rescue of a functional phenotype, particularly in the UC line. These results collectively demonstrate that TRF2 overexpression can extend beyond telomere protection and provide morphological and functional advantages to DMD iPSC-CMs.

Discussion

This study shows that treatment with TRF2 prevents telomere attrition and restores morphological deficits observed in DMD iPSC-CMs. Our previous findings in mice revealed that shortening the telomeres of dystrophin-deficient *mdx*^{4cv} mice by breeding *mdx*^{4cv} to *mTR* knockout mice provides a “humanized” model to study the severe phenotypes of Duchenne muscular dystrophy. The resulting *mdx*^{4cv}/*mTR*^{G2} mice exhibit severe skeletal muscle degeneration, kyphosis, atrophied diaphragms, dilated cardiomyopathy, and die prematurely (5–7). In histological sections of human heart tissue, telomeres are shorter in DMD patient cardiomyocytes compared to age-matched healthy controls (8), underscoring the role of telomere attrition in DMD etiology. To further understand the role of telomere shortening in the

demise of DMD cardiomyocytes, we used human iPSCs as a disease model. Previously, we characterized telomere attrition, poor calcium handling, and contractile dysfunction in DMD iPSC-CMs (10). Here we show that DMD iPSC-CMs also exhibit morphological deficits in cell size, nuclear size, and sarcomere density. We also validate telomere attrition by Southern blot of telomere restriction fragments, which reinforces our previous findings measured by quantitative fluorescent in situ hybridization and monochrome multiplex quantitative PCR (8, 10).

Previously, we reported that subunits of the shelterin complex are expressed at lower levels in DMD iPSC-CM compared to healthy controls (10). TRF2, a subunit of the shelterin complex, can repress the ATM-mediated DNA damage response (26, 27), inhibit binding of poly(ADP-ribose) polymerase 1 (PARP1) to telomeres (32), and prevent hyperresection of telomeres by exonucleases (33). Using human iPSC-CMs, we show that overexpression of TRF2 not only prevents telomere attrition but improves morphological deficits in DMD iPSC-CMs and partially rescues poor calcium handling. These results suggest that preservation of telomeres regulates cell growth and maturation. The increase in cell size and sarcomere density induced by TRF2 likely contributes to the improvement in calcium handling, leading to a functional benefit for DMD iPSC-CMs. The consistency in our findings is strengthened by the use of three DMD lines and three isogenic controls where the dystrophin mutations are corrected. We observed rescue of telomere attrition and improvements in cell size, nuclear size, as well as sarcomere density by TRF2 regardless of the type of mutation, underscoring the critical role of telomeres in the etiology of DMD.

Protection of telomeres by TRF2 can potentially be a therapeutic strategy to ameliorate other cardiovascular diseases where we and others have observed telomere attrition (8, 30, 34). Whether TRF2 overexpression can rescue disease phenotypes in iPSC-CMs harboring mutations in other proteins that make up the contractile apparatus remains to be elucidated. TRF2 is amenable to gene therapy as the coding sequence can easily fit into adeno-associated virus (35). Future studies testing TRF2 as a gene therapy in DMD animal models, such as our mdx^{4cv}/mTR^{G2} mouse model, which faithfully phenocopies dilated cardiomyopathy as seen in patients, would be important to determine efficacy beyond the cellular level. While TRF2 does not replace the function of dystrophin, we hypothesize that delivery of TRF2 can delay the premature loss of cardiomyocytes and prevent the fibrosis that accelerates the onset of dilated cardiomyopathy. Our results demonstrate that TRF2 provides a cellular advantage to DMD iPSC-CMs irrespective of the type of mutation and highlights protection of telomeres as a novel therapeutic target for other cardiomyopathies manifesting telomere attrition.

Materials and Methods

Differentiation to Cardiomyocytes

For maintenance of iPSCs, cells were seeded on Matrigel (Corning 356231)-coated plates and were cultured in Nutristem media (Reprocell 01-0005) with daily media change. For differentiation to cardiomyocytes, iPSCs were cultured to 70-90% confluency and cultured in RPMI-1640 supplemented

with 1X B27 minus insulin and 4-6 μM CHIR-99021 (Selleck S2924). Two days later, cells were refreshed with RPMI-1640 supplemented with 1X B27 minus insulin and 5 μM IWR-1 (Sigma-Aldrich I0161). Two days later, cells were refreshed in RPMI-1640 supplemented with 1X B27 minus insulin. Two days later, cells were refreshed in RPMI-1640 supplemented with 1X B27 and maintained for 4 days with a media change every other day. From day 10 of differentiation onward, iPSC-CMs were maintained in RPMI-1640 minus glucose supplemented with 1X B27 and 4 mM lactate (Sigma-Aldrich L7900) with media change every other day. On Day 10, iPSC-CMs were transduced with TRF2 or an empty control retrovirus with 8 μg/mL polybrene. Media was changed every two days. On Day 15, cells were harvested with Accutase:TrypLE (1:1 v/v) and replated on Matrigel-coated plates in RPMI-1640 minus glucose supplemented with 1X B27, 4 mM lactate, 5% KSR, and 10 μM Y-27632. On Day 16, iPSC-CMs were transduced with TNNT2-zeo. On Day 18-19, cardiomyocytes were selected for resistance to zeocin (20 μg/mL). All assays were performed on Day 30 of differentiation.

Cloning Viral Vectors

The pLPC-Empty plasmid was generated from pLPC-TRF2, a gift from Titia de Lange (Addgene plasmid #18002). TNNT2-Zeo and TNNT2-GFP were generated from TroponinT-GCaMP5-Zeo, a gift from John Gearhart (Addgene plasmid #46027).

Virus Production

Retrovirus was produced in Phoenix Amphotropic cells by transfection with FUGENE 6 (Promega E2692) of pLPC-TRF2 or pLPC-Empty. Lentivirus was produced in HEK293T cells by transfection with FUGENE 6 of TNNT2-Zeo or TNNT2-GFP-Zeo, psPAX2 packaging, and pMD2.G envelope plasmids. Media containing virus as harvested 78 hours post-transfection. Retrovirus or lentivirus was concentrated using Lenti-X Concentrator (Takara Bio 631231) using the manufacturer's protocol.

Immunofluorescence

For immunostaining, iPSCs or Day 27 iPSC-CMs were seeded onto glass slides coated with Matrigel. Three days later, cells were fixed in 4% paraformaldehyde in PBS for 15 minutes. Cells were blocked and permeabilized in buffer (20% goat serum, 0.3% Triton X-100 in PBS) for 1 hour at room temperature. Cells were incubated in primary antibody for 2 hours at room temperature or overnight at 4ºC, then washed 3 x 5 minutes in PBS. Cells were stained with the following antibodies: cardiac troponin T (Thermo Fisher MA5-12960, 1:200 dilution), dystrophin (Abcam 15277; 1:200 dilution), dystrophin (DSHB MANEX1A; 1:200 dilution), OCT4 (Millipore MAB4419; 1:100 dilution), SOX2 (BD Pharmingen 561593; 1:100 dilution), or TRA-1-60 (ESI-BIO ST11016; 1:100 dilution). Cells were incubated with secondary antibody for 1 hour at room temperature, then washed 3 x 5 minutes in PBS, with the final two washes containing 3 nM DAPI. Coverslips were mounted with Fluoromount-G (Southern Biotech 0100-01). Images were acquired on Everest deconvolution workstation (Intelligent Imaging Innovations) equipped

with a Zeiss AxioImager Z1 microscope and a CoolSnapHQ cooled CCD camera (Roper Scientific). A 20X NA0.5 Plan-Apochromat objective lens (Zeiss 420762-9800) or 63X NA1.4 Plan-Apochromat objective lens (Zeiss 420780-9900) were used to capture micrographs. Deconvolution of 3D micrographs taken at 63X were processed with Microvolution.

Western Blot

Cells were flash frozen and lysed in lysis buffer (50 mM Tris-HCl, pH 7.5, 150 mM NaCl, 1% Triton X-100, 0.1% Na deoxycholate). 25 µg of total protein was loaded on a NuPAGE Bis-Tris gel using 1X NuPAGE buffer and beta-mercaptoethanol (2.5% final concentration). Gel was run in MOPS buffer for 1-2 hours at 100V. A wet transfer to nitrocellulose membrane was done using NuPAGE Transfer Buffer at 4ºC. Membrane was blocked in 5% milk for 1 hour, then in primary antibody (TRF2 Novus NB100-56506 at 1:500; GAPDH Cell Signaling D16H11 at 1:1000) overnight 4ºC, and Goat anti Mouse IgG-HRP at 1:4000 (Thermo Fisher Scientific 62-652-0) or Goat anti Rabbit IgG-HRP at 1:2000 secondary antibody for 1 hour. Between incubations membrane was washed 3 x 10 minutes in Tris Buffered Saline with 0.1% Tween-20. Membrane was imaged by chemiluminescence (Nacalai Tesque 07880) on a Bio-Rad ChemiDoc MP System.

Flow Cytometry

iPSCs were pulsed with 20 µM EdU for 1 hour using the Click-iT EdU Alexa Fluor 647 Flow kit (Thermo Fisher C10424). iPSC-CMs were pulsed with 10 µM EdU for 24 hours. Cells were stained with LIVE/DEAD Fixable Red Dead Cell Stain (Thermo Fisher L23102) using manufacturer's protocol before fixing in 4% paraformaldehyde. Click-iT labeling of EdU was performed using manufacturer's protocol. iPSCs were stained with OCT4 (Millipore MAB4419; 1:100 dilution) and iPSC-CMs were stained with cardiac troponin T (Thermo Fisher MA5-12960, 1:200 dilution) for 1 hour at room temperature. Cells were incubated with goat-anti-rabbit Alexa 488 (Jackson ImmunoResearch 111-546-045, 1:250 dilution) for 30 minutes at room temperature. DNA was stained with FxCycle Violet Flow Reagent (Thermo Fisher R37166) using manufacturer's protocol. Four-color flow cytometry analysis was performed on the SONY SH800 using unstained samples and fluorescence minus one controls to set detectors. FlowJo v10 was used to analyze flow cytometry data.

Acknowledgments

We are grateful to David L. Mack, Martin K. Childers, and Chris Denning for providing the iPSC lines. We acknowledge Garry P. Nolan for providing the Phoenix Amphotropic cells. This work was supported by the American Heart Association (18POST33960526 to A.E. and 17CSA33590101 to H.M.B.), Stanford School of Medicine Dean's Postdoctoral Fellowship (A.E.), Stanford Translational Research and Applied Medicine Pilot Grant (A.E.), the Stanford Bio-X Summer Undergraduate Research Program (F.B.), a Major Grant from the Stanford University Vice Provost for Undergraduate Education (F.B.), the National

Institutes of Health HL159340 (H.M.B.), the Keck Foundation (H.M.B.), the Baxter Foundation (H.M.B.), and the Li Ka Shing Foundation (H.M.B.). For statistical analysis, we consulted the Stanford's Data Studio, supported by the National Center for Advancing Translational Sciences of the National Institutes of Health under Award Number UL1TR003142.

Author Contributions: A.E. and H.M.B. designed research; A.E. and K.K. performed research; A.E., K.K., and S.I.T.B. analyzed data; F.B. contributed new analytic tools; and A.E. and H.M.B. wrote the paper.

Competing Interest Statement: The authors declare no competing interest.

References

1. E. M. McNally, *et al.*, Contemporary cardiac issues in Duchenne muscular dystrophy. *Circulation* **131**, 1590–1598 (2015).
2. T. L. E. van Westering, C. A. Betts, M. J. A. Wood, Current understanding of molecular pathology and treatment of cardiomyopathy in duchenne muscular dystrophy. *Mol. Basel Switz.* **20**, 8823–8855 (2015).
3. G. Nigro, L. I. Comi, L. Politano, R. J. Bain, The incidence and evolution of cardiomyopathy in Duchenne muscular dystrophy. *Int. J. Cardiol.* **26**, 271–277 (1990).
4. F. Kamdar, D. J. Garry, Dystrophin-Deficient Cardiomyopathy. *J. Am. Coll. Cardiol.* **67**, 2533–2546 (2016).
5. A. Sacco, *et al.*, Short telomeres and stem cell exhaustion model Duchenne muscular dystrophy in mdx/mTR mice. *Cell* **143**, 1059–1071 (2010).
6. F. Mourkioti, *et al.*, Role of telomere dysfunction in cardiac failure in Duchenne muscular dystrophy. *Nat. Cell Biol.* **15**, 895–904 (2013).
7. A. C. Y. Chang, *et al.*, Telomere shortening and metabolic compromise underlie dystrophic cardiomyopathy. *Proc. Natl. Acad. Sci. U. S. A.* **113**, 13120–13125 (2016).
8. A. C. Y. Chang, *et al.*, Telomere shortening is a hallmark of genetic cardiomyopathies. *Proc. Natl. Acad. Sci. U. S. A.* **115**, 9276–9281 (2018).
9. C. V. Theodoris, *et al.*, Long telomeres protect against age-dependent cardiac disease caused by NOTCH1 haploinsufficiency. *J. Clin. Invest.* **127** (2017).
10. A. C. Y. Chang, *et al.*, Increased tissue stiffness triggers contractile dysfunction and telomere shortening in dystrophic cardiomyocytes. *Stem Cell Rep.* **16**, 1–13 (2021).
11. H. Wu, *et al.*, Modelling diastolic dysfunction in induced pluripotent stem cell-derived cardiomyocytes from hypertrophic cardiomyopathy patients. *Eur. Heart J.* **40**, 3685–3695 (2019).
12. J. Z. Zhang, *et al.*, A Human iPSC Double-Reporter System Enables Purification of Cardiac Lineage Subpopulations with Distinct Function and Drug Response Profiles. *Cell Stem Cell* **24**, 802-811.e5 (2019).
13. C. L. Bladen, *et al.*, The TREAT-NMD DMD global database: analysis of more than 7,000 Duchenne muscular dystrophy mutations. *Hum. Mutat.* **36**, 395–402 (2015).
14. E. Dick, *et al.*, Two new protocols to enhance the production and isolation of human induced pluripotent stem cell lines. *Stem Cell Res.* **6**, 158–167 (2011).
15. E. Dick, *et al.*, Exon skipping and gene transfer restore dystrophin expression in human induced pluripotent stem cells-cardiomyocytes harboring DMD mutations. *Stem Cells Dev.* **22**, 2714–2724 (2013).
16. X. Guan, *et al.*, Dystrophin-deficient cardiomyocytes derived from human urine: new biologic reagents for drug discovery. *Stem Cell Res.* **12**, 467–480 (2014).
17. J. M. Pioner, *et al.*, Absence of full-length dystrophin impairs normal maturation and contraction of cardiomyocytes derived from human-induced pluripotent stem cells. *Cardiovasc. Res.* **116**, 368–382 (2020).
18. R. W. Kaspar, *et al.*, Analysis of dystrophin deletion mutations predicts age of cardiomyopathy onset in Becker muscular dystrophy. *Circ. Cardiovasc. Genet.* **2**, 544–551 (2009).
19. X. Lian, *et al.*, Robust cardiomyocyte differentiation from human pluripotent stem cells via temporal modulation of canonical Wnt signaling. *Proc. Natl. Acad. Sci. U. S. A.* **109**, E1848-57 (2012).

20. S. Tohyama, *et al.*, Distinct metabolic flow enables large-scale purification of mouse and human pluripotent stem cell-derived cardiomyocytes. *Cell Stem Cell* **12**, 127–137 (2013).

21. R. C. Austin, P. L. Howard, V. N. D'Souza, H. J. Klamut, P. N. Ray, Cloning and characterization of alternatively spliced isoforms of Dp71. *Hum. Mol. Genet.* **4**, 1475–1483 (1995).

22. S. Jelinkova, *et al.*, DMD Pluripotent Stem Cell Derived Cardiac Cells Recapitulate in vitro Human Cardiac Pathophysiology. *Front. Bioeng. Biotechnol.* **8**, 535 (2020).

23. A. J. S. Ribeiro, *et al.*, Contractility of single cardiomyocytes differentiated from pluripotent stem cells depends on physiological shape and substrate stiffness. *Proc. Natl. Acad. Sci. U. S. A.* **112**, 12705–12710 (2015).

24. D. T. Paik, M. Chandy, J. C. Wu, Patient and Disease-Specific Induced Pluripotent Stem Cells for Discovery of Personalized Cardiovascular Drugs and Therapeutics. *Pharmacol. Rev.* **72**, 320–342 (2020).

25. S. Wakai, *et al.*, Electron microscopic study of the biopsied cardiac muscle in Duchenne muscular dystrophy. *J. Neurol. Sci.* **84**, 167–175 (1988).

26. J. Karlseder, *et al.*, The telomeric protein TRF2 binds the ATM kinase and can inhibit the ATM-dependent DNA damage response. *PLoS Biol.* **2**, E240 (2004).

27. E. L. Denchi, T. de Lange, Protection of telomeres through independent control of ATM and ATR by TRF2 and POT1. *Nature* **448**, 1068–1071 (2007).

28. R. C. Addis, *et al.*, Optimization of direct fibroblast reprogramming to cardiomyocytes using calcium activity as a functional measure of success. *J. Mol. Cell. Cardiol.* **60**, 97–106 (2013).

29. P. J. Wrighton, *et al.*, Signals from the surface modulate differentiation of human pluripotent stem cells through glycosaminoglycans and integrins. *Proc. Natl. Acad. Sci. U. S. A.* **111**, 18126–18131 (2014).

30. H. Oh, *et al.*, Telomere attrition and Chk2 activation in human heart failure. *Proc. Natl. Acad. Sci. U. S. A.* **100**, 5378–5383 (2003).

31. J. N. Weiss, A. Garfinkel, H. S. Karagueuzian, P.-S. Chen, Z. Qu, Early afterdepolarizations and cardiac arrhythmias. *Heart Rhythm* **7**, 1891–1899 (2010).

32. I. Schmutz, L. Timashev, W. Xie, D. J. Patel, T. de Lange, TRF2 binds branched DNA to safeguard telomere integrity. *Nat. Struct. Mol. Biol.* **24**, 734–742 (2017).

33. F. Lottersberger, A. Bothmer, D. F. Robbiani, M. C. Nussenzweig, T. de Lange, Role of 53BP1 oligomerization in regulating double-strand break repair. *Proc. Natl. Acad. Sci.* **110**, 2146–2151 (2013).

34. V. Codd, *et al.*, Polygenic basis and biomedical consequences of telomere length variation. *Nat. Genet.* **53**, 1425–1433 (2021).

35. D. Wang, P. W. L. Tai, G. Gao, Adeno-associated virus vector as a platform for gene therapy delivery. *Nat. Rev. Drug Discov.* **18**, 358–378 (2019).

Supplementary Information Appendix

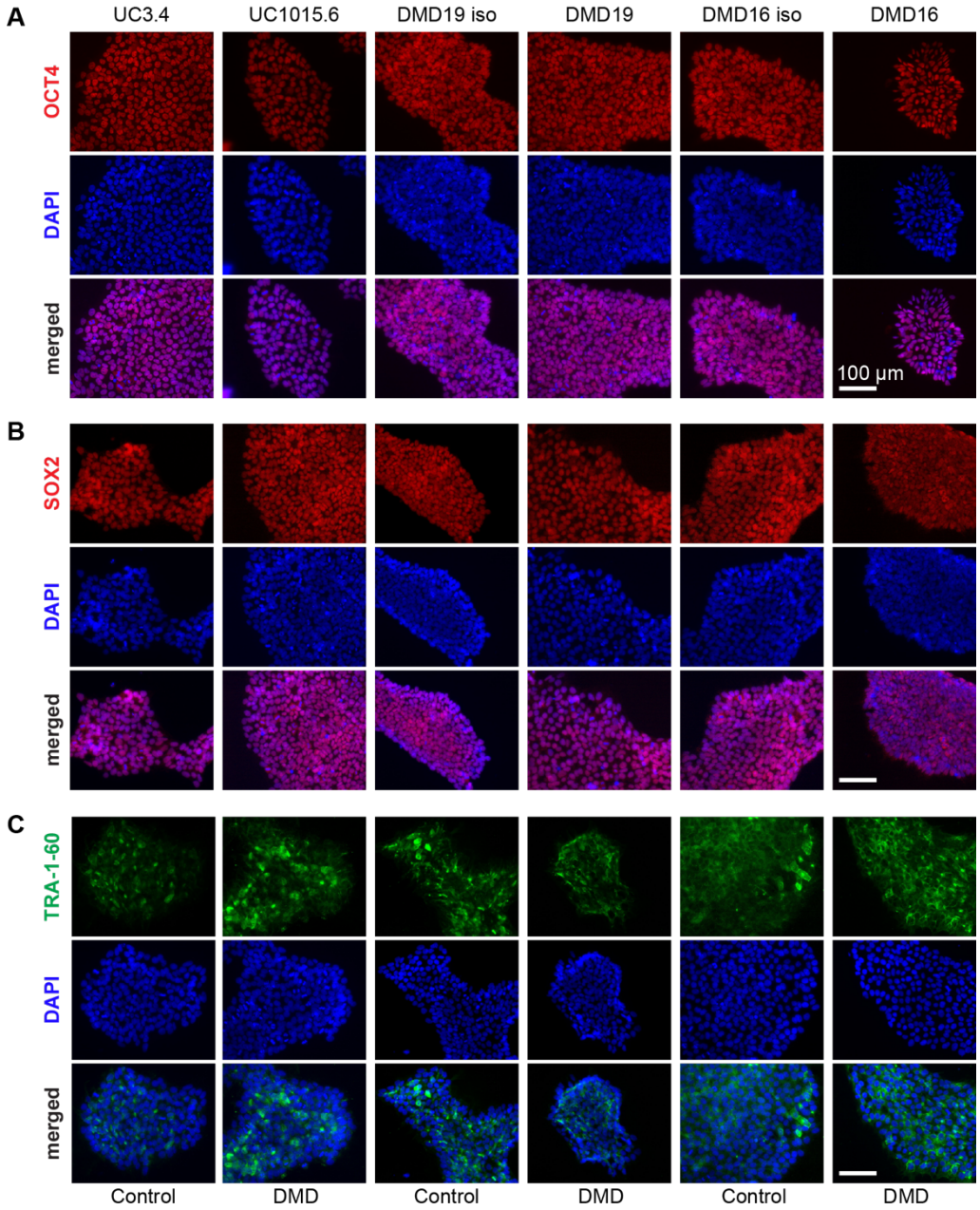

Figure S1. Markers of pluripotency expressed by iPSCs. Immunostaining for (*A*) OCT4, (*B*) SOX2, and (*C*) TRA-1-60. Scale bar = 100 µm.

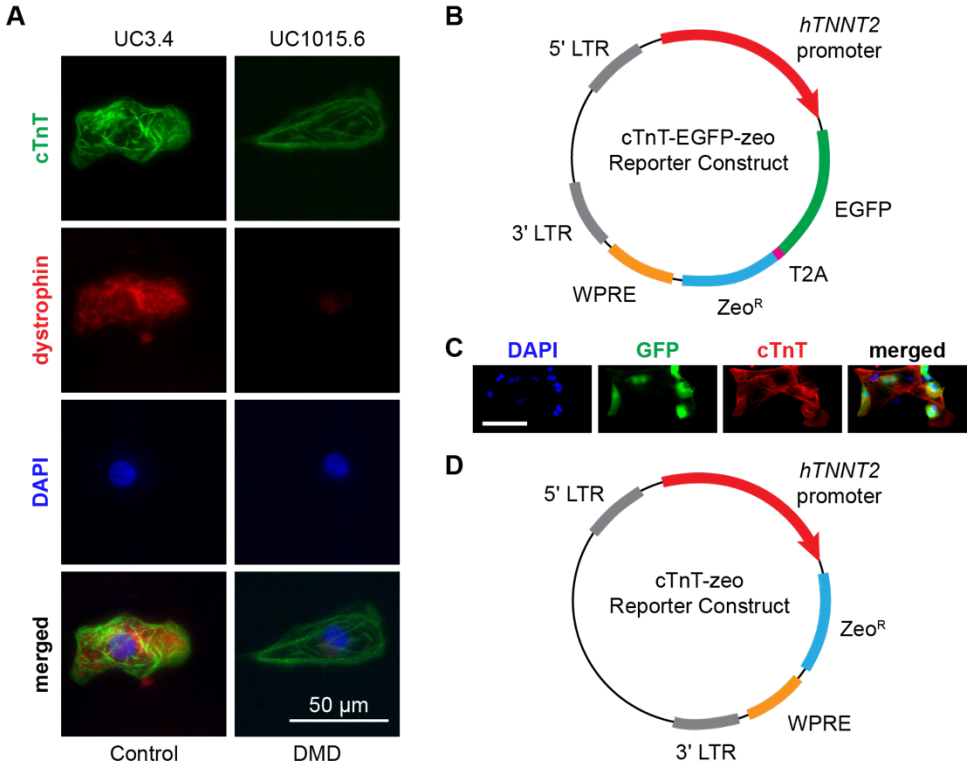

Figure S2. Cardiomyocyte markers in iPSC-CMs. (*A*) Immunostaining for dystrophin in Day 30 iPSC-CMs using the MANEX1A antibody that recognizes the N-terminus. Cardiac troponin T is a cardiac-specific marker. DAPI marks nuclei. Scale bar = 50 µm. (*B*) Cardiac troponin T reporter construct. The human troponin T promoter drives expression of the bicistronic cassette that expresses EGFP and the zeocin resistance gene separated by a T2A self-cleaving peptide. (*C*) EGFP reporter in iPSC-CMs immunostained for cardiac troponin T. DAPI marks nuclei. Scale bar = 100 µm. (*D*) Non-fluorescent cardiac troponin T reporter construct. The human troponin T promoter drives expression of the zeocin resistance gene only.

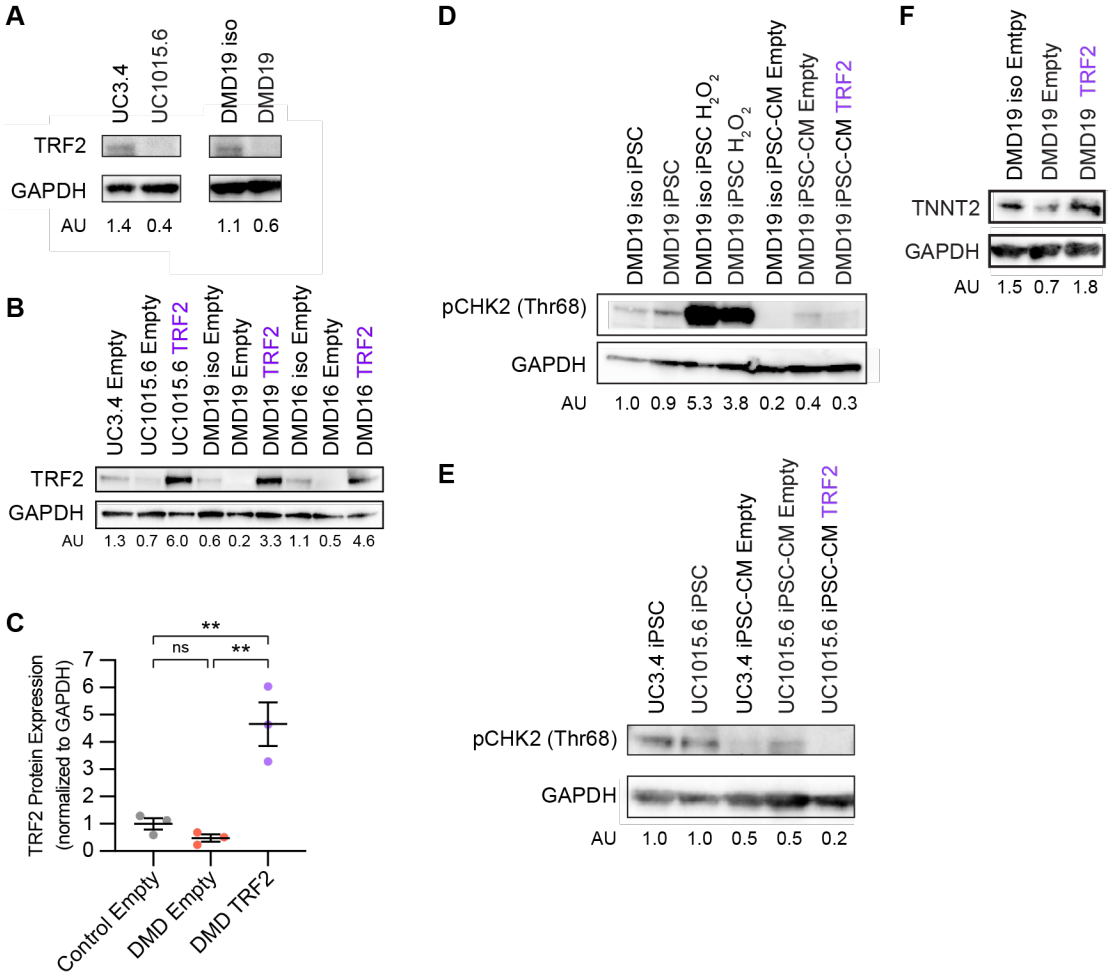

Figure S3. TRF2 attenuates activation of ATM-mediated DNA damage response. (*A*) Western blot of TRF2 levels with GAPDH as a loading control. TRF2 signal normalized to GAPDH signal in arbitrary units. (*B*) TRF2 expression data from the western blot in (*C*). Data shown are mean ± SEM. One-way ANOVA and Tukey test for post-hoc comparison was used to calculate significance. ** $p < 0.01$. (*C*) Western blot of TRF2 levels with GAPDH as a loading control in Day 30 iPSC-CMs. TRF2 signal normalized to GAPDH signal in arbitrary units. (*D*) Western blot of cardiac troponin T (TNNT2) levels with GAPDH as a loading control in Day 30 iPSC-CMs. TNNT2 signal normalized to GAPDH signal in arbitrary units. (*E*) Western blot of phospho-CHK2 (pCHK2) (Thr68) for iPSCs and Day 30 iPSC-CMs in the DMD19 lines.(*F*) Western blot of pCHK2 for iPSCs and Day 30 iPSC-CMs in the UC lines. pCHK2 signal normalized to GAPDH signal in arbitrary units.

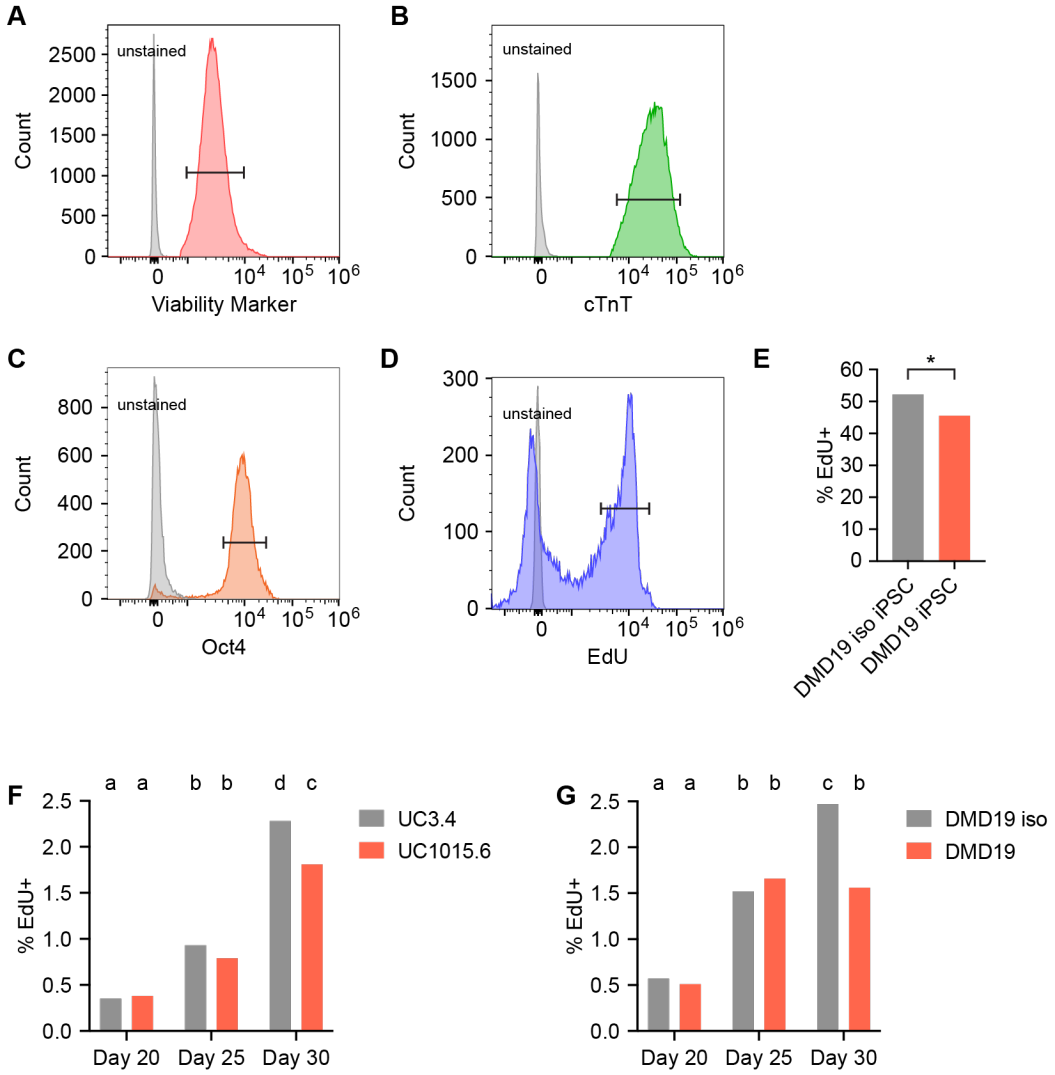

Figure S4. Small fraction of iPSC-CMs incorporate EdU. Flow cytometry was performed and gated for (*A*) cell viability using a LIVE/DEAD Fixable Dead Cell Stain, (*B*) cardiac troponin T for cardiomyocytes, (*C*) OCT4 for iPSCs, and (*D*) EdU. (*E*) Percentage of EdU+ cells in iPSCs. DMD19 iso, N = 37,743 cells; DMD19, N = 75,913 cells. * $p < 0.05$. (*F*) Percentage of EdU+ cells in UC iPSC-CMs. UC3.4 Day 20, N = 23,814 cells; UC1015.6 Day 20, N = 101,557 cells; UC3.4 Day 25, N = 25,578 cells; UC1015.6 Day 25, N = 79,862 cells; UC3.4 Day 30, N = 10,694 cells; UC1015.6 Day 30, N = 40,394 cells. (*G*) Percentage of EdU+ cells in DMD19 iPSC-CMs at the indicated day of differentiation. DMD19 iso Day 20, N = 74,392 cells; DMD19 Day 20, N = 135,985 cells; DMD19 iso Day 25, N = 50,588 cells; DMD19 Day 25, N = 79,610 cells; DMD19 iso Day 30, N = 35,696 cells; DMD19 Day 30, N = 39,397 cells. Different letters denote statistically significant different frequencies. $p < 0.05$. Pearson's chi-square test was used to compare frequencies of EdU+ cells. Z-test with Bonferroni correction was used for pairwise comparisons. n = 3 biological replicates.

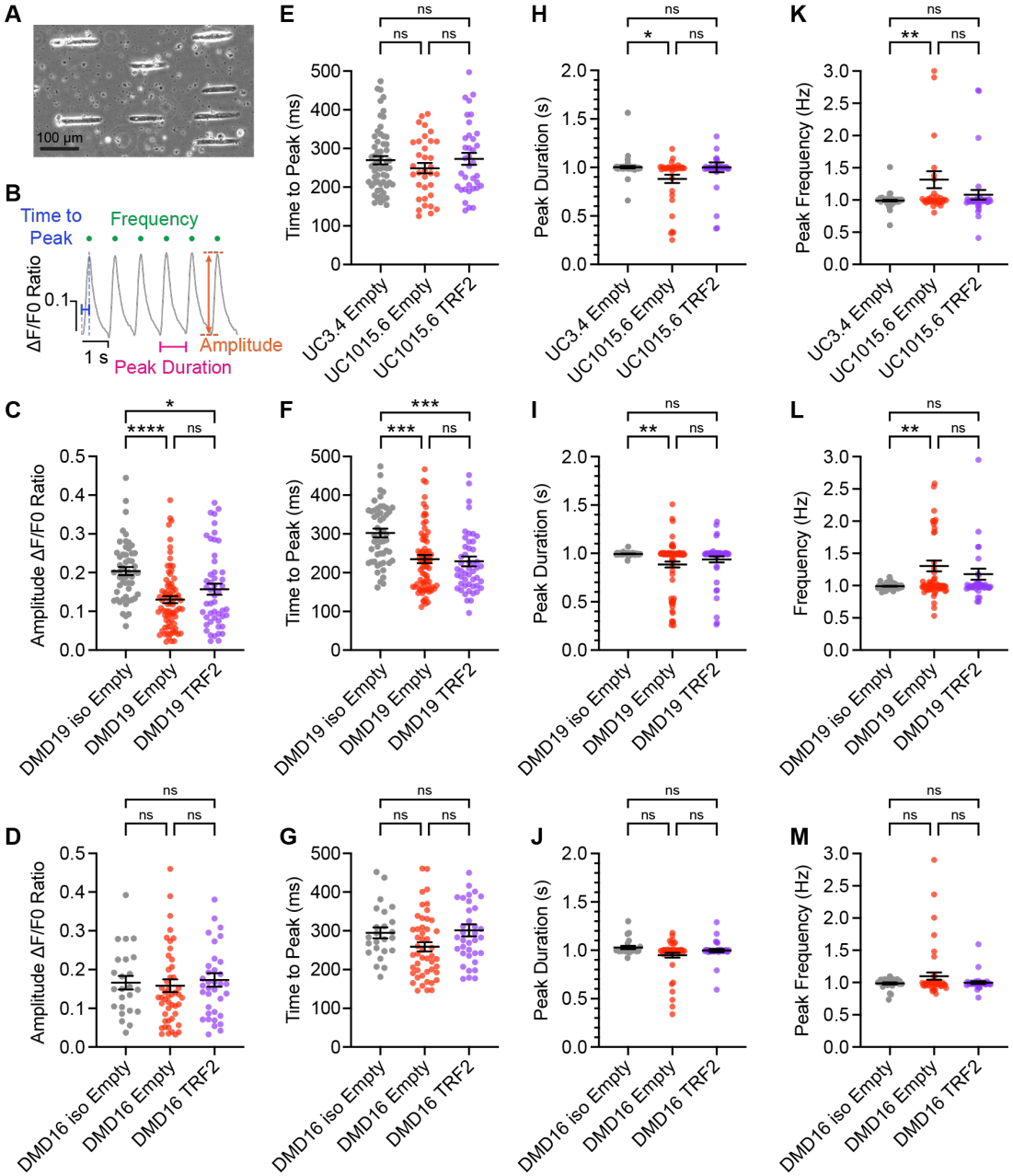

Figure S5. Effects of TRF2 on calcium handling of Day 30 iPSC-CMs paced at 1 Hz. Cells were transduced with TRF2 or an empty retroviral control. (*A*) Micropatterning of iPSC-CMs to a 7:1 length:width aspect ratio promotes maturation by parallel alignment of the myofibrils and adoption of a physiologically-relevant morphology. (*B*) Parameters of calcium handling. Amplitude is the difference between the maximum and minimum calcium ratio. Time to peak is the duration of time from minimum to maximum. Peak duration is the duration of time from minimum to the next minimum. Peak frequency is the rate of oscillations per second. 1 Hertz (Hz) is equal to 1 cycle per second. Amplitude for (*C*) DMD19 iPSC-CMs and (*D*) DMD16 iPSC-CMs. Time to peak for (*E*) UC iPSC-CMs, (*F*) DMD19 iPSC-CMs, and (*G*) DMD16 iPSC-CMs. Peak duration for (*H*) UC iPSC-CMs, (*I*) DMD19 iPSC-CMs, and (*J*) DMD16 iPSC-CMs. Peak frequency for (*K*) UC iPSC-CMs, (*L*) DMD19 iPSC-CMs, and (*M*) DMD16 iPSC-CMs. Cells were scored from 3-6 differentiation experiments. Calcium imaging was performed on 24-77 cells per condition. Data shown are mean ± SEM. One-way ANOVA and Tukey test for post-hoc comparison was used to determine significance. * $p < 0.05$, ** $p < 0.01$, and **** $p < 0.0001$.

Table S1. Chi-squared test for Figure 5*D-F*.

Fig. 5*D*	df = 4		Condition		
			UC3.4 Empty	UC1015.6 Empty	UC1015.6 TRF2
	Class I	Count	47	13	19
		% within Condition	79.7%	38.2%	52.8%
		Adjusted Residual	3.942	-3.208	-1.227
		Corrected P-value	0.0007	0.0120	1.9784
	Class II	Count	10	10	10
		% within Condition	16.9%	29.4%	27.8%
		Adjusted Residual	-1.557	0.990	0.756
		Corrected P-value	1.0752	2.8996	4.0468
	Class III	Count	2	11	7
		% within Condition	3.4%	32.4%	19.4%
		Adjusted Residual	-3.490	3.163	0.769
		Corrected P-value	0.0043	0.0140	3.977
	Total	Count	59	34	36

Fig. 5*E*	df = 4		Condition		
			DMD19 iso Empty	DMD19 Empty	DMD19 TRF2
	Class I	Count	49	32	24
		% within Condition	92.5%	41.6%	48.0%
		Adjusted Residual	5.998	-3.947	-1.744
		Corrected P-value	0.00000	0.0007	0.7304
	Class II	Count	4	22	18
		% within Condition	7.5%	28.6%	36.0%
		Adjusted Residual	-3.408	1.114	2.237
		Corrected P-value	0.0059	2.3875	0.2275
	Class III	Count	0	23	8
		% within Condition	0.0%	29.9%	16.0%
		Adjusted Residual	-3.953	3.886	-0.269
		Corrected P-value	0.0007	0.0009	7.0913
	Total	Count	53	77	50

Fig. 5*F*	df = 4		Condition		
			DMD16 iso Empty	DMD16 Empty	DMD16 TRF2
	Class I	Count	17	27	21
		% within Condition	70.8%	56.3%	58.3%
		Adjusted Residual	1.208	-0.747	-0.278
		Corrected P-value	2.0434	4.0956	7.0291
	Class II	Count	7	13	13
		% within Condition	29.2%	27.1%	36.1%
		Adjusted Residual	-0.167	-0.701	0.886
		Corrected P-value	7.8063	0.3497	3.3805
	Class III	Count	0	8	2
		% within Condition	0.0%	16.7%	5.6%
		Adjusted Residual	-1.774	2.375	-0.939
		Corrected P-value	0.685	0.158	3.1296
	Total	Count	24	48	36